



# A cation-regulation strategy for achieving high-performance perovskite solar cells via a fully-evaporation process

Zhiwen Niu<sup>a</sup>, Ting Lei<sup>b,\*,\*\*</sup>, Hua Dong<sup>b</sup>, Zhouhu Deng<sup>a,\*\*\*</sup>, Wu Zhao<sup>a</sup>, Feihong Li<sup>a</sup>, Siwei Ye<sup>b</sup>, Zhaoxin Wu<sup>b,c,\*</sup>

<sup>a</sup> School of Information Science and Technology, Northwest University, Xi'an, Shanxi, 710069, China

<sup>b</sup> Key Laboratory of Photonics Technology for Information, Key Laboratory for Physical Electronics and Devices of the Ministry of Education, School of Electronic Technology and Engineering, Xi'an Jiaotong University, Xi'an, 710049, China

<sup>c</sup> Collaborative Innovation Center of Extreme Optics, Shanxi University, Taiyuan, 030006, China

## ARTICLE INFO

### Keywords:

Perovskite solar cells  
Cs dopant  
Fully-evaporation technology  
Large-area module  
Stability

## ABSTRACT

Mixed-cation halide perovskite solar cells (PSCs) have received extensive attention due to their excellent optoelectronic properties and long-term stability. How to further promote its facile and large-scale film-formation procedure is of great significance for commercialization. In this work, a CsMA-based perovskite film was prepared via a two-step evaporation process. By regulating the cation ratio systematically, uniform and large-scale perovskite films can be obtained with excellent stability and high crystallization. Based on the perovskite active layer, typical PSCs were developed with a fully-evaporation technology, and the power conversion efficiency (PCE) of the champion device is 17.15% ( $J_{SC} = 22.59 \text{ mA cm}^{-2}$ ,  $V_{OC} = 1.03 \text{ V}$ ,  $FF = 73.71\%$ ). In addition, the PSC module was also explored (active area  $\approx 10 \text{ cm}^2$ ), achieving a PCE of 10.24%. It prospects that our efforts could draw inspiration for pushing ahead the industrialization of the perovskite photovoltaic.

## 1. Introduction

In the past ten years, hybrid organic-inorganic perovskites have become one of the most popular optoelectronic materials due to their excellent optical properties, including adjustable bandgap, high carrier mobility, and excellent semiconducting properties [1–6]. The critical factors in improving the power conversion efficiency (PCE) of perovskite solar cells (PSCs) are the crystallinity of perovskite film [7–11], the adjustment of perovskite composition [12–16], and the optimization of the device structure [17–21]. Up to now, the highest PCE of the PSCs certified by the authorized agency has reached 25.2% [22]. However, the instability of the PSCs and the loss of PCE in amplifying the active device region still limit the development of perovskite cells in commercial applications [23–25].

As one of the commonly used crystal structures of perovskite materials, methylammonium lead iodide ( $\text{CH}_3\text{NH}_3\text{PbI}_3$ ,  $\text{MAPbI}_3$ ) has been widely used in perovskite solar cells. However, the stability of  $\text{MAPbI}_3$  is poor since its crystal lattice is easily destroyed, especially under

conditions of high temperature and humidity [24]. In response to this problem, many methods have been proposed, such as reducing the defects of the perovskite crystal [26], using a stable inorganic charge transport layer [27], and improving the encapsulation process [28]. In fact, adjusting the composition of perovskites is also an effective method. For instance, Br ions are introduced into perovskites and partially substituted for I ions to form dense, stable structures [29]. Some alkali metal cations such as Cs cations are used to partially replace MA cations, reducing MA vacancy defects and inhibiting ion migration [30]. However, these improvements are based on the solution method, which is sensitive to the environment and difficult to apply to large-area film preparation. Therefore, it is necessary to develop more innovative strategies for preparing stable and large-area PSCs.

Nowadays, the preparation of perovskite films by vacuum deposition has received wide attention owing to its facial process to produce smooth, evenly covered films [31–35]. Snaith et al. explored preparing perovskite films by dual-source evaporation in 2013 [2]. Lin et al. proposed a sequential vacuum deposition method to control the proportion

\* Corresponding author. Key Laboratory of Photonics Technology for Information, Key Laboratory for Physical Electronics and Devices of the Ministry of Education, School of Electronic Technology and Engineering, Xi'an Jiaotong University, Xi'an, 710049, China.

\*\* Corresponding author.

\*\*\* Corresponding author.

E-mail addresses: [leiting512@stu.xjtu.edu.cn](mailto:leiting512@stu.xjtu.edu.cn) (T. Lei), [dengzh@nwu.edu.cn](mailto:dengzh@nwu.edu.cn) (Z. Deng), [zhaoxinwu@mail.xjtu.edu.cn](mailto:zhaoxinwu@mail.xjtu.edu.cn) (Z. Wu).

of deposition accurately [36]. Meanwhile, a work based on mixed chemical vapor deposition was reported to form MAPbI<sub>3</sub> perovskites by sequential deposition [37]. Recently, in order to improve the performance of MAPbI<sub>3</sub> perovskite solar cells based on vapor deposition, cation doping methods are being explored continuously. A mixed vapor of FAI and MAI reacts with lead iodide film to form (FA)<sub>x</sub>(MA)<sub>1-x</sub>PbI<sub>3</sub> perovskite, which could increase short circuit current density [38]. A film blended with lead iodide and cesium iodide forms a stable perovskite film by reacting with MA vapor [39]. Preparation of Cs<sub>0.5</sub>FA<sub>0.4</sub>MA<sub>0.1</sub>Pb(I<sub>0.83</sub>Br<sub>0.17</sub>)<sub>3</sub> perovskite compounds by simultaneous evaporation with multiple evaporation sources was reported [40]. The above researches have made good progress in improving PCE based on small-area device. However, these methods have not been conducted in large-area modules.

In this work, a Cs<sub>x</sub>MA<sub>1-x</sub>PbI<sub>3</sub> perovskite film which has compact grains and no pin-holes was prepared through sequential two-step evaporation techniques. Meanwhile, we developed a fully-evaporation method to prepare PSCs devices and successfully applied this method to the preparation of large-area modules. It should be noticed that at the optimum Cs doping concentration, the defect density of the perovskite films can be effectively reduced while the recombination resistance increases significantly. The champion device based on Cs<sub>x</sub>MA<sub>1-x</sub>PbI<sub>3</sub> reaches a PCE of 17.15% and shows prominent stability. More importantly, a PSC module with a PCE of 10.24% can be prepared on a substrate with an area of 10.8 cm<sup>2</sup>, which demonstrates the feasibility of the method for preparing large-area and high-quality films.

## 2. Experimental

### 2.1. Materials

PbI<sub>2</sub> (99.999 wt%) and CsI (99.999 wt%) was purchased from Alfa Aesar and used as received. MAI was synthesized as reported previously. Vanadium triisopropoxy oxide (96%) was purchased from Alfa Aesar and diluted before use. C<sub>60</sub> was purchased from xi'an Polymer Light Technology Corp. BCP was purchased from Nichem. Dimethyl formamide (DMF) and 2-Propanol (IPA) were purchased from Sinopharm Chemical Reagent Co. Ltd.

### 2.2. Device fabrication

ITO-coated glasses used as substrates were cleaned with detergent, deionized water, and acetone in order for 15 min, and then exposed to ultraviolet ozone plasma for 10 min after drying. First, the substrates were transferred into a vacuum chamber and the vacuum pressure was reduced to below  $6 \times 10^{-6}$  mbar before evaporation. VO<sub>x</sub> and CuPc were sequentially deposited at a deposition rate of  $0.5 \text{ \AA s}^{-1}$ , and the thickness of VO<sub>x</sub> layer was 10 nm covered with a CuPc layer of 10 nm. Then the samples were transferred to another vacuum chamber to complete the deposition of the perovskite film, and the vacuum pressure is maintained at  $3 \times 10^{-6}$  mbar to  $6 \times 10^{-6}$  mbar. The PbI<sub>2</sub> and the CsI were simultaneously evaporated on the substrates at a calculated fixed rate. In order to obtain films with Cs-to-Pb stoichiometry ratios of 0.03, 0.05, 0.07, and 0.1, PbI<sub>2</sub> was deposited at a thickness of 200 nm with a deposition rate of  $3.9 \text{ \AA s}^{-1}$ , and the deposition rates of CsI were  $0.09 \text{ \AA s}^{-1}$ ,  $0.15 \text{ \AA s}^{-1}$ ,  $0.21 \text{ \AA s}^{-1}$ ,  $0.3 \text{ \AA s}^{-1}$ . After the evaporative crucible cooled down, the MAI coated on the molybdenum foil was rapidly vaporized onto the prepared film of PbI<sub>2</sub> - CsI mixture when the evaporation current momentarily reached 100 A in a few seconds. In order to ensure the uniformity and sufficiency of the reaction, it is necessary to distribute MAI evenly on the molybdenum foil. MAI powder was first dissolved in DMF. Then MAI solution was uniformly coated on a molybdenum foil. After that, molybdenum foil is placed on the annealing plate to remove excess DMF solution. Apart from this, the distance between the substrate and the molybdenum foil was about 5 cm. After that, the films were transferred to a nitrogen-filled glove box and placed on a

hot plate through a vacuum transition chamber, annealed at 100 °C for 30 min and gradually transforming into the Cs<sub>x</sub>MA<sub>1-x</sub>PbI<sub>3</sub> perovskite. After the perovskite films cooled down, the excess MAI was removed by soaking the samples in the IPA solution for 10 s. Then the excess IPA on the film was blown off with N<sub>2</sub> gas. Finally, the samples were transferred into a vacuum chamber and the chamber was evacuated to a pressure of  $6 \times 10^{-6}$  mbar. LiF, C<sub>60</sub>, BCP and silver were sequentially deposited on the perovskite films at an evaporation rate of  $0.1 \text{ \AA s}^{-1}$ ,  $0.35 \text{ \AA s}^{-1}$ ,  $0.1 \text{ \AA s}^{-1}$ , and  $0.5 \text{ \AA s}^{-1}$  with thicknesses of 1 nm, 30 nm, 6 nm, and 120 nm, respectively.

### 2.3. Characterization

**Film Characterization:** The morphology and roughness of the perovskite films were investigated by a field emission scanning electron microscope (SEM; Quanta 250, FEI, USA) and an atomic force microscope (AFM; Digital Instruments Dimension 3100 scanning force microscope). XRD measurements were tested with an X-ray diffractometer (D/MAX-2400, Rigaku, Japan) with Cu K $\alpha$  radiation. The absorption spectra was obtained by UV-vis spectrophotometer (HITACHI U-3010, Japan). The PL spectra was recorded on a fluorescence spectrometer (Fluoromax-4 spectrofluorometer). And the time-resolved PL spectra was recorded on an FLS920 spectrometer through a time-correlated single-photon counting system.

**Device Characterization:** The area of each device was calibrated uniformly through a 7.00 square millimeter mask and all tests were carried out in ambient air. The photovoltaic performance was evaluated under an AM 1.5 G illumination of  $100 \text{ mW cm}^{-2}$  with an AAA solar simulator (XES-301, SAN-EI). The photocurrent-voltage (J-V) curve was obtained by a Keithley (2602 Series Sourcemeter) with a scan rate of  $0.01 \text{ V s}^{-1}$  step. Incident photon-to-current conversion efficiency spectra was collected in a DC mode by a solar cell quantum efficiency measurement system (SolarCellScan 100, Zolix Instruments. Co. Ltd.). Capacitance - Voltage (C-V), space charge limited current (SCLC) and electrochemical impedance spectra (EIS) of the devices were measured by CHI-660E.

## 3. Results and discussion

Fig. 1 shows the preparation method of the perovskite films, including sequential deposition and annealing. For the first step, ratio-tuned PbI<sub>2</sub> and CsI were deposited on the substrate through a co-evaporation process. Subsequently, organic salt MAI was flash-vaporized onto the mixed film. Finally, a high-quality hybrid film was formed after annealing.

By adjusting the evaporative rates of CsI and PbI<sub>2</sub>, a series of perovskites can be obtained with different ratios of Cs-to-Pb, including 0, 0.03, 0.05, 0.07, 0.1. The effect of Cs dopant on the morphology of Cs<sub>x</sub>MA<sub>1-x</sub>PbI<sub>3</sub> perovskite is investigated by observing the surface morphology of the films. As shown in Fig. 2a–e, all perovskite films are uniform and flat, forming dense grain boundaries and completely covering the hole transport layer without pinholes. It can be seen that the pristine perovskite surface consists of many small grains due to the poor crystallinity (Fig. 2a). Obviously, the introduction of Cs affects the morphology of perovskite films. When the concentration of Cs increases from 0 to 0.05, the grains of the films become larger and smoother in general, which is conducive to effectively hindering carrier recombination and reducing defects, as well as enhancing the ability of charge transfer between interfaces. Because grain boundaries usually consist of defects, larger grain size means less grain boundary density, which means less photoelectric loss. However, as the concentration of Cs continues to increase, the grain size of the perovskite films tends to decrease overall. The element distribution mapping is shown in Fig. S1, which can prove the uniform distribution of Cs on the surface of the films by evaporation. In the meanwhile, a cross-sectional SEM image of the device with ITO/VO<sub>x</sub>/CuPc/perovskite/LiF/C<sub>60</sub>/BCP/Ag structure is

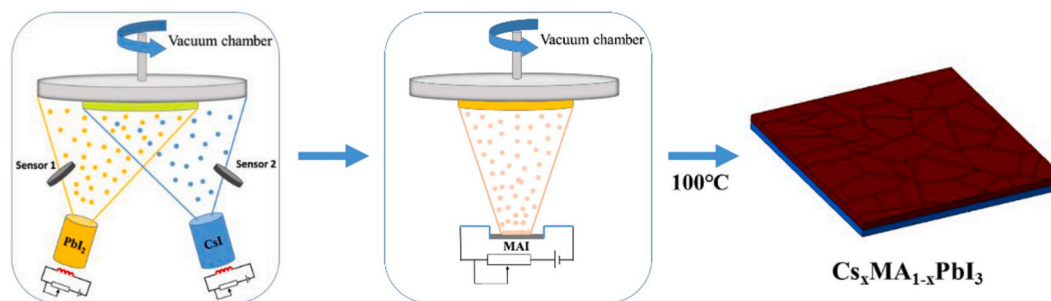


Fig. 1. Schematic illustration of the two-step evaporation method used for preparing the  $\text{Cs}_x\text{MA}_{1-x}\text{PbI}_3$  perovskite.

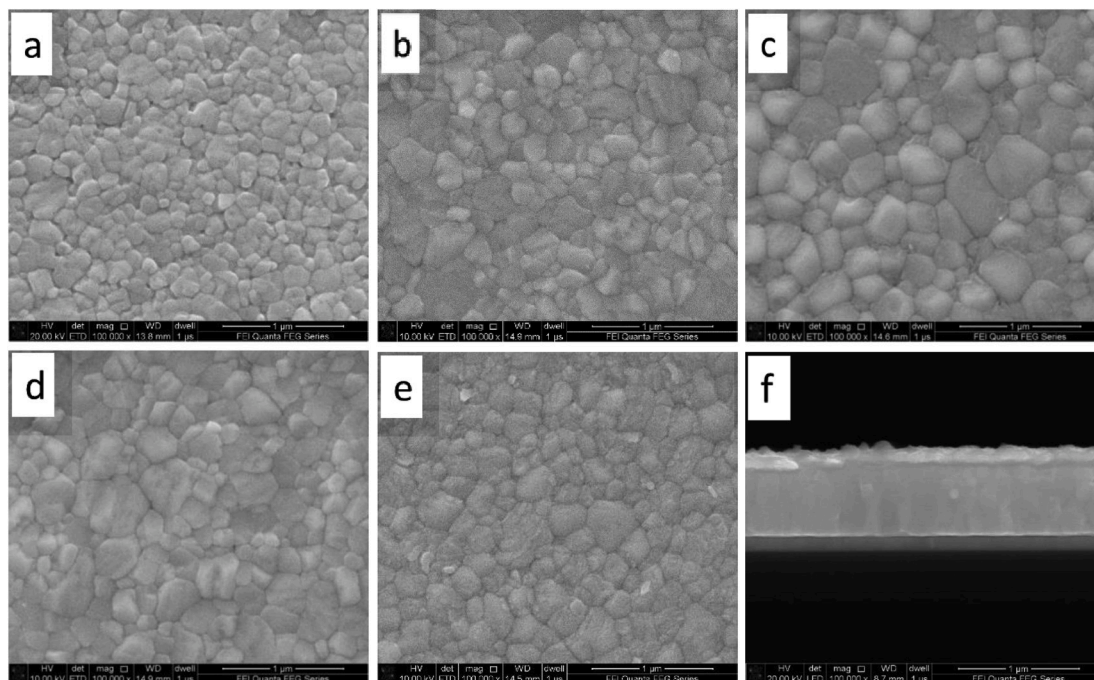


Fig. 2. (a)–(e) SEM images of the  $\text{Cs}_x\text{MA}_{1-x}\text{PbI}_3$  perovskite with different Cs amounts from 0 to 0.1. (f) A cross-sectional SEM image of  $\text{Cs}_x\text{MA}_{1-x}\text{PbI}_3$  device.

shown in Fig. 2f. The overall thickness of the device is about 650 nm, and the perovskite layer with a thickness of 380 nm is immensely coherent, which can be clearly distinguished from other functional layers. The elemental distribution of the cross-section is shown in Fig. S2, which reflects the homogeneous incorporation of Cs and I into the perovskite film.

In order to investigate the crystallization of the  $\text{Cs}_x\text{MA}_{1-x}\text{PbI}_3$  perovskite with different Cs contents, X-ray diffraction (XRD) measurements are carried out on these films. As shown in Fig. 3a, it is apparent that all samples exhibit strong crystallinity and show no apparent  $\text{PbI}_2$  characteristic peaks at  $12.8^\circ$ , indicating that the reaction was complete and there is no residue of the  $\text{PbI}_2$ . The perovskite diffraction peaks of these samples including (110), (220) crystal planes reveal the existence of the tetragonal phase of perovskite. The magnified view of the (110) diffraction peak is shown in Fig. 3b. As the concentration of Cs increases, the intensity and angle of (110) diffraction peak slightly change. The strongest (110) diffraction peak is obtained when the ratio of Cs-to-Pb is 5%, indicating that the crystallinity and crystal orientation of samples are in optimal condition. It was reported that the introduction of Cs is beneficial to reduce the bulk defect density of solar cells [41]. The diffraction angle of perovskite in (110) plane shifts from  $14.09^\circ$  to larger angle, because of the difference in ionic radius between  $\text{Cs}^+$  (1.81 Å) and  $\text{MA}^+$  (2.70 Å) [42], which indicates that  $\text{Cs}^+$  effectively replace  $\text{MA}^+$  and the lattice constant decreases accordingly. With the

proportion of Cs increasing to 10%, there is no evidence that the emergence of characteristic peaks of  $\text{CsPbI}_3$ , indicating that no phase separation has occurred.

The optical properties of  $\text{Cs}_x\text{MA}_{1-x}\text{PbI}_3$  with different proportions of Cs are characterized by UV–Vis analysis, as shown in Fig. 3c. All samples exhibit significant absorption edges around 780 nm. It should be noticed that with the increase of Cs content, the absorption edge of the samples moves toward the shorter wavelength slightly. What is more, the bandgap of the  $\text{Cs}_x\text{MA}_{1-x}\text{PbI}_3$  film is estimated by the Tauc plot. As shown in Fig. S3, the band gaps of the samples are found to rise from 1.587 eV to 1.599 eV with adding Cs content.

In order to prove that the introduction of Cs has a positive effect on the crystallinity of  $\text{MAPbI}_3$  perovskite, all samples deposited on the glass are measured by steady-state photoluminescence (PL) with an excitation wavelength of 532 nm (Fig. 3d). It can be observed that all the perovskite films show an emission wavelength around 766 nm. When the Cs content reaches 5%, the PL strength of samples shows the strongest peak, which is mainly due to the fewer traps. As the increase of the Cs content, PL strength decreases slightly due to the lattice mismatch caused by excessive Cs.

The influence of Cs introduction on perovskite can be further studied by testing X-ray photoelectron spectroscopy, as shown in Fig. S4. As is clear from Fig. S5a, the characteristic peak of Cs 3d is not detected. When the content of Cs reaches 0.05, two distinct characteristic peaks



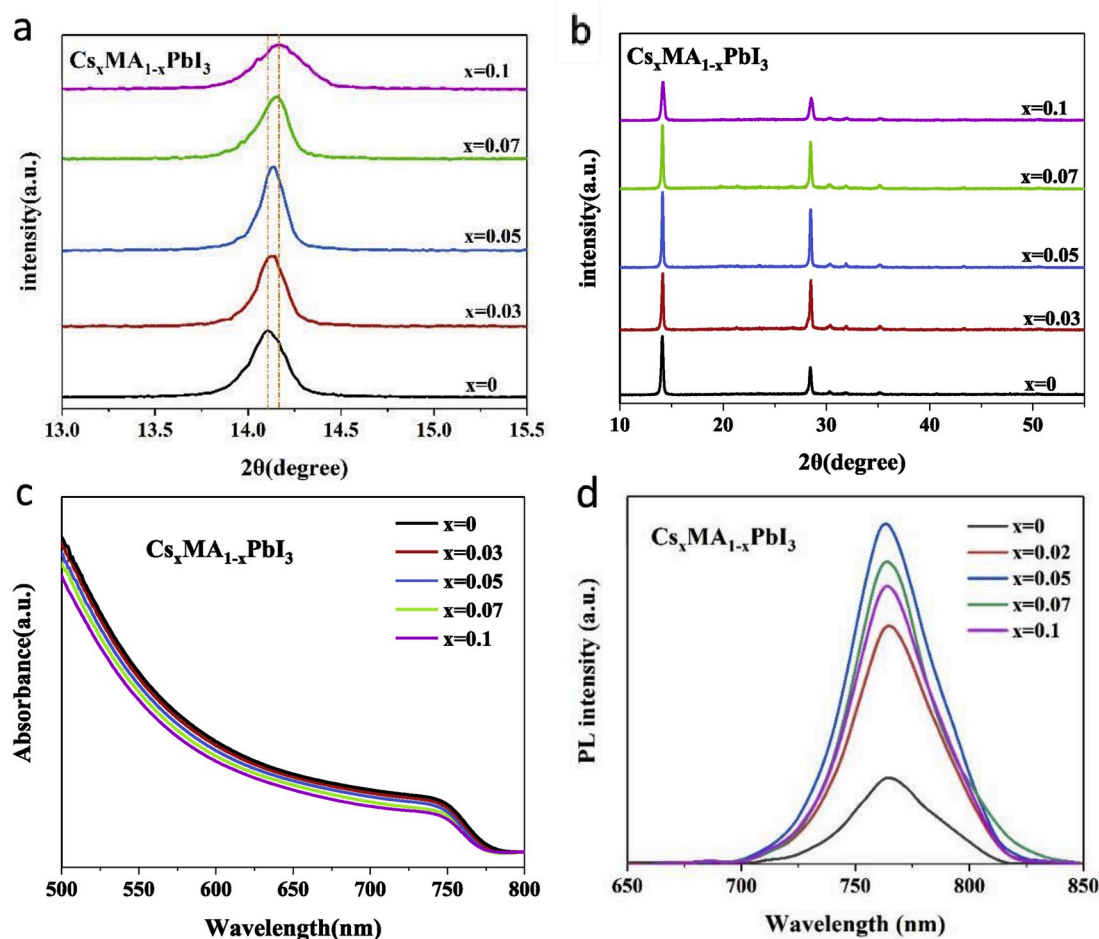


**Fig. 3.** (a) XRD patterns of the  $\text{Cs}_x\text{MA}_{1-x}\text{PbI}_3$  films. (b) A magnified view of the XRD (110) diffraction peak corresponding to the  $\text{Cs}_x\text{MA}_{1-x}\text{PbI}_3$  films. (c) UV-Vis absorption spectra and (d) PL spectra of  $\text{Cs}_x\text{MA}_{1-x}\text{PbI}_3$  films deposited on glass substrates.

appear at 738.0 eV and 724.0 eV, corresponding to Cs  $3d_{3/2}$  and Cs  $3d_{5/2}$ . As shown in Fig. S5b and Fig. S5c, without the introduction of Cs, the Pb 4f peak and I 3d peak are detected at 142.3 eV, 137.4 eV, 629.8 eV, and 618.3 eV, corresponding to Pb  $4f_{5/2}$ , Pb  $4f_{7/2}$ , I  $3d_{3/2}$  and I  $3d_{5/2}$ , respectively. Meanwhile, the presence of Cs causes the Pb 4f peak and I 3d peak to shift to higher binding energy, which means that the lattice parameters decrease slightly, and the results are consistent with the conclusion drawn by the previous analysis of XRD.

Based on the high-quality perovskite film described above, we fabricated a full-evaporation PSC with a conventional multilayer planar structure of ITO/ $\text{VO}_x$ /CuPc/perovskite/LiF/ $\text{C}_{60}$ /BCP/Ag, where the hybrid hole transport layer was reported in the previous work [43]. We found that 1 nm LiF deposited between perovskite and  $\text{C}_{60}$  improves the  $V_{OC}$  and FF of the devices. It will inhibit the nonradiative recombination of interfaces between perovskite and  $\text{C}_{60}$  [44]. Fig. S5 shows the current-voltage (J-V) curves of the pristine  $\text{MAPbI}_3$  and  $\text{Cs}_{0.05}\text{MA}_{0.95}\text{PbI}_3$  PSCs with or without LiF, and the key parameters are listed in Table S1. The schematic diagram and the energy diagrams of the planar heterojunction device are shown in Fig. 4a. The current-voltage (J-V) curves of  $\text{Cs}_x\text{MA}_{1-x}\text{PbI}_3$  with different ratios of Cs-to-Pb are shown in Fig. 4b, and the key parameters are listed in Table 1. It can be seen that the best performance of the pristine PSC shows a PCE of 14.06%, a short circuit current density ( $J_{SC}$ ) of  $21.58 \text{ mA cm}^{-2}$ , an open circuit voltage ( $V_{OC}$ ) of 0.967 V and a fill factor (FF) of 67.37%. Notably, the existence of Cs could considerably enhance the photovoltaic performance of PSCs due to the improved quality of the perovskite film as investigated above. The electrical performance parameters ( $J_{SC}$ ,  $V_{OC}$ , FF, PCE) of  $\text{Cs}_x\text{MA}_{1-x}\text{PbI}_3$  have different degrees of

improvement when  $x = 0.05$ , among which  $V_{OC}$  and  $J_{SC}$  are the main factors affecting the rise of PCE. The parameters including  $V_{OC}$ ,  $J_{SC}$ , FF and PCE of the best performance device are 1.03 V,  $22.59 \text{ mA cm}^{-2}$ , 73.71% and 17.15%, respectively.  $V_{OC}$  depends on the bandgap of the light-absorbing layer and the loss of carrier recombination at the interface. As mentioned before, the doping of Cs into perovskite films causes a rise in the bandgap, which is one of the reasons for the improvement of  $V_{OC}$ . The second reason for the increase of  $V_{OC}$  is that larger grains effectively reduce defect traps and carrier recombination. In the meanwhile, the rise of  $J_{SC}$  and FF is mainly due to the drop of defect density, which was confirmed by the results of SCLC in subsequent sections. Fig. 4c shows that there is almost no hysteresis effect in the optimal PSC, which is attributed to the planar structure of the perovskite devices. The IPCE spectrum of the PSC device with  $\text{Cs}_{0.05}\text{MA}_{0.95}\text{PbI}_3$  and the calculated  $J_{SC}$  values are presented in Fig. 4d. It is worth noting that the IPCE fluctuates around 85% in the range of 450–750 nm and the  $J_{SC}$  ( $22.12 \text{ mA cm}^{-2}$ ) calculated by integral is close to the  $J_{SC}$  ( $22.59 \text{ mA cm}^{-2}$ ) in J-V curve. Meanwhile, Fig. S6 contains the IPCE spectrum of the PSC device with  $\text{MAPbI}_3$  and the calculated  $J_{SC}$  values. In order to study the stability of the device during operation, the stabilized maximum power output of the photocurrent density is measured at a bias of 0.81 V, as shown in Fig. 4e. It can be seen that the current density drops rapidly and then rises gradually to a steady state due to the hysteresis, remaining at  $20.83 \text{ mA cm}^{-2}$ .

TRPL can be used to characterize the photo-generated carrier lifetime in the perovskite film and reflect the trap state density of the perovskite film. As shown in Fig. 5a, a pure  $\text{MAPbI}_3$  film and a  $\text{Cs}_x\text{MA}_{1-x}\text{PbI}_3$  film with optimum doping concentration are prepared on the glass

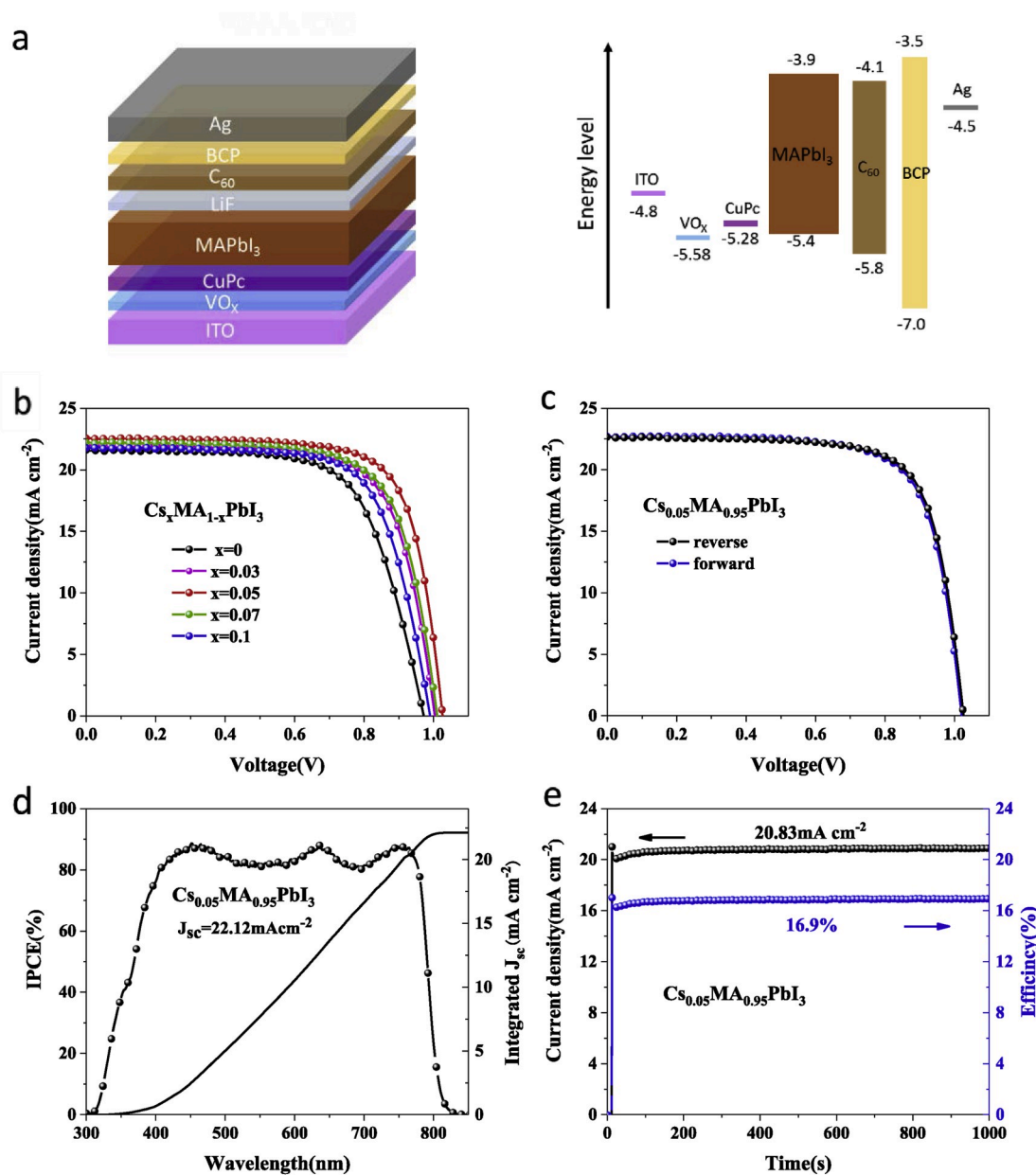


**Fig. 4.** (a) The schematic diagram and the energy diagrams of the planar heterojunction device. (b) J-V curves of the Cs<sub>x</sub>MA<sub>1-x</sub>PbI<sub>3</sub> PSCs with different x values. (c) The J-V curve of the optimum performance PSC under forward and reverse scan. (d) IPCE spectrum of the champion devices. (e) Photocurrent density and PCE measured as a function of time biased at 0.81 V for the Cs<sub>0.05</sub>MA<sub>0.95</sub>PbI<sub>3</sub> device.

**Table 1**

Key J-V parameters of the Cs<sub>x</sub>MA<sub>1-x</sub>PbI<sub>3</sub> devices.

Cs content	J <sub>sc</sub> (mA cm <sup>-2</sup> )	V <sub>oc</sub> (V)	FF(%)	PCE(%)
0	21.58	0.967	67.37	14.06
0.03	22.02	1.004	71.29	15.75
0.05	22.59	1.030	73.71	17.15
0.07	22.21	1.010	71.41	16.02
0.1	21.82	0.990	70.53	15.23

substrate and tested by the TRPL. It is apparent that the carrier lifetime of the pristine sample is lower than the carrier lifetime of the sample at Cs concentration of 0.05. The carrier lifetime significantly increases from 34.17 ns to 43.66 ns (Table S2). The rise of the lifetime is mainly due to the suppression of the recombination of photogenerated charge carriers, which is related to the reduced trap density mentioned later.

In order to explore the effect of the introduction of Cs into the

perovskite films on the defect density, we fabricated a two-electron layer device (ITO/C<sub>60</sub>/perovskite/C<sub>60</sub>/Ag) of perovskite films with different Cs content. Space charge limited current (SCLC) tests in dark conditions can reveal the intrinsic characteristics of perovskite films. As shown in Fig. 5b, the initial voltage of the trap filling limit ( $V_{TFL}$ ) of MAPbI<sub>3</sub> films is 0.91 V, and the trap state density is calculated to be  $1.75 \times 10^{16} \text{ cm}^{-3}$  according to the formula in Supporting information [45]. As the Cs content increases to 0.05,  $V_{TFL}$  drops to 0.47 V, and the corresponding density of the trap state is  $0.91 \times 10^{16} \text{ cm}^{-3}$ . These results reflect the existence of Cs may affect the reduction of the defect states density of the perovskite films to some extent.

The charge transport and recombination processes inside the device are further studied by carrying out electrical impedance spectroscopy (EIS). Fig. 5c shows the Nyquist plot of the impedance spectrum of the device tested in dark conditions. The upper right area of the figure shows the equivalent circuit of the device, consisting of sheet resistance ( $R_s$ ), recombination resistance ( $R_{rec}$ ) and capacitance of cells ( $C_{pe}$ ). The fitted

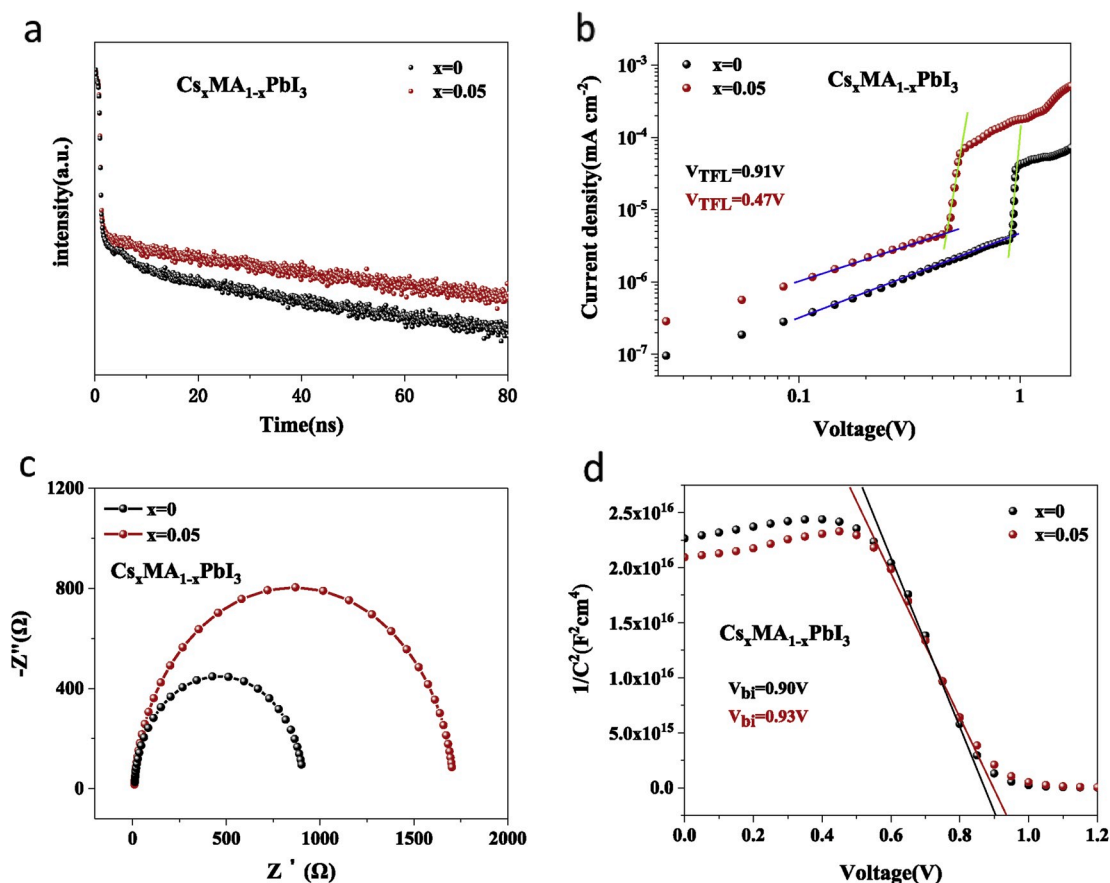


**Fig. 5.** (a) TRPL spectra of MAPbI<sub>3</sub> and Cs<sub>0.05</sub>MA<sub>0.95</sub>PbI<sub>3</sub> devices deposited on glass substrates. (b) Current density–voltage characteristics of MAPbI<sub>3</sub> and Cs<sub>0.05</sub>MA<sub>0.95</sub>PbI<sub>3</sub> for estimating the defect density. (c) EIS measurement of PSCs with MAPbI<sub>3</sub> and Cs<sub>0.05</sub>MA<sub>0.95</sub>PbI<sub>3</sub>. (d) Mott–Schottky plots of the MAPbI<sub>3</sub> and Cs<sub>0.05</sub>MA<sub>0.95</sub>PbI<sub>3</sub> devices.

results of all resistance values are collected in Table S3. It is found that the  $R_{\text{rec}}$  value increased obviously from 900.3 Ω to 1701 Ω, indicating that the charge recombination is suppressed, corresponding to the results of PL and TRPL.

Capacitance–Voltage (C–V) is characterized to analyze the cause of  $V_{\text{OC}}$  increase. According to the Mott–Schottky equation in Supporting information, the built-in potential ( $V_{\text{bi}}$ ) is related to the intercept and can be obtained by fitting the curve in the Mott–Schottky plot. The value of  $V_{\text{OC}}$  is positively correlated with the  $V_{\text{bi}}$ . As shown in Fig. 5d, the  $V_{\text{bi}}$  of the pristine device and the device with Cs content at 0.05 are calculated to be 0.90 V and 0.93 V, respectively. This increase is mainly due to the reduction in the density of defect states of perovskites, which is advantageous for inhibiting the recombination of carriers and reducing the loss of energy.

Moreover, the stabilities of the MAPbI<sub>3</sub> and Cs<sub>0.05</sub>MA<sub>0.95</sub>PbI<sub>3</sub> devices are also studied. We conducted stability tests by exposing them to air (40% RH) for half a month without encapsulation. Fig. 6a depicts the normalized PCE of the devices for 15 consecutive days. Compared with the MAPbI<sub>3</sub> device of 35% attenuation efficiency, the Cs<sub>0.05</sub>MA<sub>0.95</sub>PbI<sub>3</sub> device shows excellent stability with an efficiency attenuation of 15%. As shown in Fig. 6b, XRD measurements are carried out on the two perovskite films. It is worth noting that diffraction peaks of lead iodide appear in both samples, indicating the decomposition of the perovskite films, in which the decomposition of MAPbI<sub>3</sub> was most obvious. In fact, one of the reasons for the improved stability of Cs doped PSCs is that the defect-states density of perovskites is reduced due to the partial replacement of MA cations by Cs cations, and another reason is that the presence of Cs cations inhibits the ions migration [46].

The flatness and uniformity of the perovskite active layer and the

functional layer based on vacuum deposition are very well, which is beneficial to the promotion of the PSCs from small-area to large-area. The high PCE of the module depends on the uniform distribution of the large-area device with excellent photoelectric performance. We have made statistics on the electrical performance parameters of the MAPbI<sub>3</sub> and Cs<sub>0.05</sub>MA<sub>0.95</sub>PbI<sub>3</sub> devices, and the distribution statistics are shown in Fig. S7. Compared with all parameters distribution range of the standard PSCs, the parameters distribution range of Cs doped PSCs is narrower, which is related to the reduction of defect-state density calculated in previous sections.

Ultimately, we fabricated a PSC module based on the fully-evaporation process. As shown in Fig. 6c and Fig. S8, the PSC module with an effective area of 10.8 cm<sup>2</sup> consists of eight sub-PSCs with an effective area of 1.35 cm<sup>2</sup> (0.30 cm × 4.5 cm). The sub-PSCs are connected in series by effectively masking each functional layer and the distance between adjacent sub-PSCs is 5.6 cm. Fig. 6d shows the best performance of the champion module with a PCE of 10.24%, a  $V_{\text{oc}}$  of 7.73 V, a  $J_{\text{sc}}$  of 1.96 mA cm<sup>-2</sup> and a FF of 67.9% under reverse scanning.

#### 4. Conclusion

In summary, we fabricated high-quality Cs<sub>x</sub>MA<sub>1-x</sub>PbI<sub>3</sub> perovskite films by a sequential two-step evaporation method. By optimizing the content of Cs, the properties of the perovskite films can be significantly improved, such as larger and smoother grains, lower defect density, and higher recombination resistance. As a result, the PCE of the champion device reaches 17.15%, which is about 20% higher than that of the standard device. The stability of the Cs doped PSCs is also improved, and the PCE of the champion device is only attenuated by 15% within half a

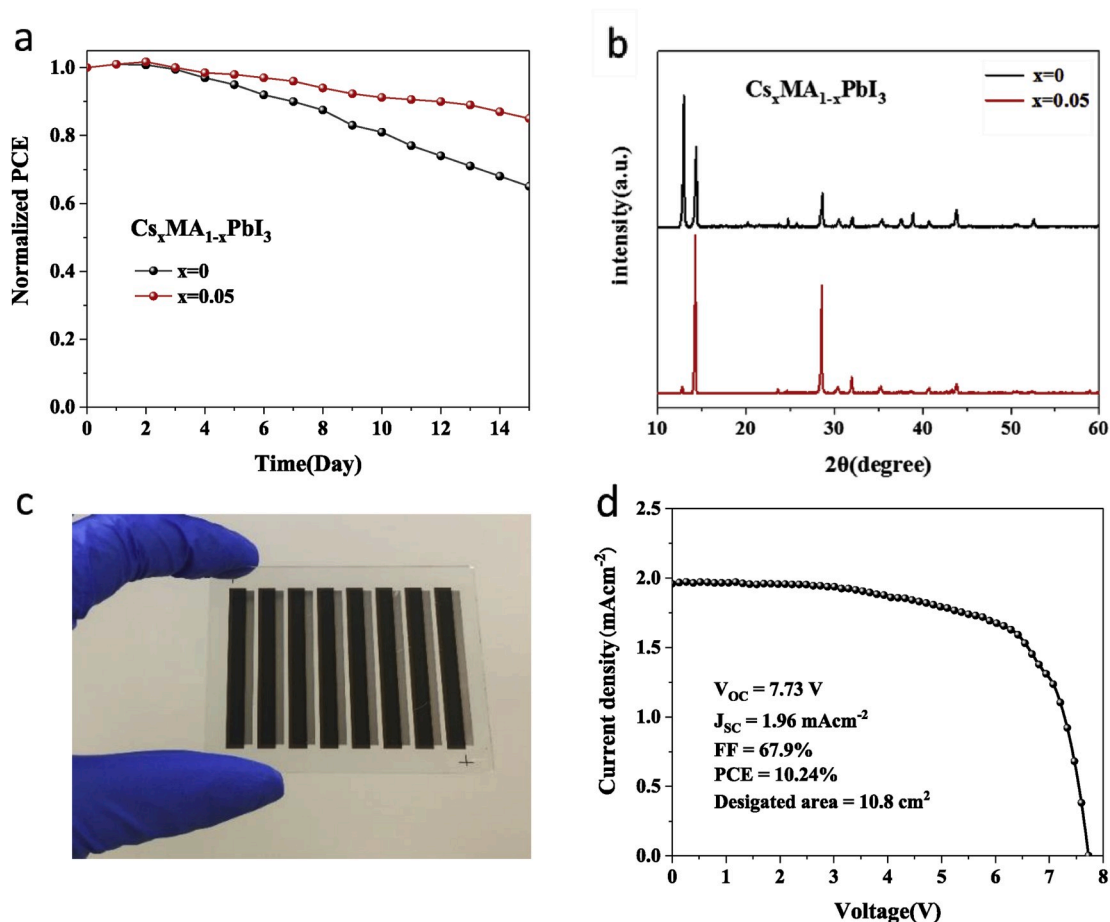


Fig. 6. (a) The long-term stability test of  $\text{MAPbI}_3$  and  $\text{Cs}_{0.05}\text{MA}_{0.95}\text{PbI}_3$  device stored in ambient condition (40% RH) without encapsulation. (b) XRD patterns of the  $\text{MAPbI}_3$  and  $\text{Cs}_{0.05}\text{MA}_{0.95}\text{PbI}_3$  films placed in ambient condition (40% RH) without encapsulation after half a month. (c) Image of a  $\text{Cs}_{0.05}\text{MA}_{0.95}\text{PbI}_3$  module with an effective area of  $10.8 \text{ cm}^2$  (8 sub-cells in series). (d) J-V curve of the champion  $\text{Cs}_{0.05}\text{MA}_{0.95}\text{PbI}_3$  module.

month. It is worth noting that the existence of Cs effectively improves the uniformity of the device, which is one of the important factors restricting the PCE of large-area modules. The PCE of a PSC module based on Cs dopant with an active area of  $10.8 \text{ cm}^2$  can reach 10.24%. These results show that we provide a new method to prepare PSC modules for large areas.

#### Declaration of competing interest

The authors declare that they have no known competing financial interests or personal relationships that could have appeared to influence the work reported in this paper.

#### Acknowledgements

This work was financially supported by National Natural Science Foundation of China (Grant Nos. 61604121, 61935016), Natural Science Basic Research Plan in Shaanxi Province of China (Grant Nos. 2019JQ-119, 2017JM5135), and Fundamental Research Funds for the Central Universities (Grant No. xjj2016031). The SEM work was performed at the International Center by Dielectric Research (ICDR), Xi'an Jiaotong University, Xi'an, China. The authors thank Mr. Ma and Mrs. Dai for their help in using SEM.

#### Appendix A. Supplementary data

Supplementary data to this article can be found online at <https://doi.org/10.1016/j.orgel.2020.105710>.

#### References

- [1] A. Kojima, K. Teshima, Y. Shirai, T. Miyasaka, Organometal halide perovskites as visible-light sensitizers for photovoltaic cells, *J. Am. Chem. Soc.* 131 (2009) 6050–6051.
- [2] M. Liu, M.B. Johnston, H.J. Snaith, Efficient planar heterojunction perovskite solar cells by vapour deposition, *Nature* 501 (2013) 395–398.
- [3] Y.Q. Zu, J. Xi, L. Li, J.F. Dai, S.P. Wang, F. Yun, B. Jiao, H. Dong, X. Hou, Z.X. Wu, High-brightness and color-tunable  $\text{FAPbBr}_3$  perovskite nanocrystals 2.0 enable ultrapure green luminescence for achieving recommendation 2020 displays, *ACS Appl. Mater. Interfaces* 12 (2020) 2835–2841.
- [4] N.J. Jeon, J.H. Noh, W.S. Yang, Y.C. Kim, S. Ryu, J. Seo, S.I. Seok, Compositional engineering of perovskite materials for high-performance solar cells, *Nature* 517 (2015) 476–480.
- [5] J.X. Jinfei Dai, Yanqing Zu, Li Lu, Jie Xu, Yifei Shi, Xiaoyun Liu, Qinhua Fan, Junjie Zhang, ShuangPeng Wang, Fang Yuan, Hua Dong, Bo Jiao, Xun Hou, Zhaoxin Wu, Surface mediated ligands addressing bottleneck of room-temperature synthesized inorganic perovskite nanocrystals toward efficient light-emitting diodes, *Nano Energy* 70 (2020).
- [6] J. Burschka, N. Pellet, S.J. Moon, R. Humphry-Baker, P. Gao, M.K. Nazeeruddin, M. Gratzel, Sequential deposition as a route to high-performance perovskite-sensitized solar cells, *Nature* 499 (2013) 316–319.
- [7] H. Dong, Z.X. Wu, J. Xi, X.B. Xu, L.J. Zuo, T. Lei, X.G. Zhao, L.J. Zhang, X. Hou, A. K.Y. Jen, Pseudohalide-Induced recrystallization engineering for  $\text{CH}_3\text{NH}_3\text{PbI}_3$  film and its application in highly efficient inverted planar heterojunction perovskite solar cells, *Adv. Funct. Mater.* 28 (2018).
- [8] B. Danekamp, N. Droseros, F. Palazon, M. Sessolo, N. Banerji, H.J. Bolink, Efficient photo- and electroluminescence by trap states passivation in vacuum-deposited hybrid perovskite thin films, *ACS Appl. Mater. Interfaces* 10 (2018) 36187–36193.
- [9] J. Xi, K. Xi, A. Sadhanala, K.H.L. Zhang, G.R. Li, H. Dong, T. Lei, F. Yuan, C.X. Ran, B. Jiao, P.R. Coxon, C.J. Harris, X. Hou, R.V. Kumar, Z.X. Wu, Chemical sintering reduced grain boundary defects for stable planar perovskite solar cells, *Nano Energy* 56 (2019) 741–750.
- [10] C. Li, J. Yin, R. Chen, X. Lv, X. Feng, Y. Wu, J. Cao, Monoammonium porphyrin for blade-coating stable large-area perovskite solar cells with >18% efficiency, *J. Am. Chem. Soc.* 141 (2019) 6345–6351.



- [11] J.B. Chen, J.K. Ren, Z.F. Li, H. Wang, Y.Y. Hao, Mixed antisolvents assisted treatment of perovskite for photovoltaic device efficiency enhancement, *Org. Electron.* 56 (2018) 59–67.
- [12] X. Xu, C. Ma, Y.-M. Xie, Y. Cheng, Y. Tian, M. Li, Y. Ma, C.-S. Lee, S.-W. Tsang, Air-processed mixed-cation  $\text{Cs}_{0.15}\text{FA}_{0.85}\text{PbI}_3$  planar perovskite solar cells derived from a  $\text{PbI}_2\text{-CsI-FAI}$  intermediate complex, *J. Mater. Chem. A* 6 (2018) 7731–7740.
- [13] G.Q. Tong, H. Li, G.P. Li, T. Zhang, C.D. Li, L.W. Yu, J. Xu, Y. Jiang, Y. Shi, K. J. Chen, Mixed cation perovskite solar cells by stack-sequence chemical vapor deposition with self-passivation and gradient absorption layer, *Nano Energy* 48 (2018) 536–542.
- [14] J. Xi, Z.X. Wu, B. Jiao, H. Dong, C.X. Ran, C.C. Piao, T. Lei, T.B. Song, W.J. Ke, T. Yokoyama, X. Hou, M.G. Kanatzidis, Multichannel interdiffusion driven FASnI (3) film formation using aqueous hybrid salt/polymer solutions toward flexible lead-free perovskite solar cells, *Adv. Mater.* 29 (2017) 7.
- [15] L. Luo, Y. Zhang, N. Chai, X. Deng, J. Zhong, F. Huang, Y. Peng, Z. Ku, Y.-B. Cheng, Large-area perovskite solar cells with  $\text{Cs}_x\text{FA}_{1-x}\text{PbI}_{3-y}\text{Br}_y$  thin films deposited by a vapor–solid reaction method, *J. Mater. Chem. A* 6 (2018) 21143–21148.
- [16] X. Zhu, D. Yang, R. Yang, B. Yang, Z. Yang, X. Ren, J. Zhang, J. Niu, J. Feng, S. F. Liu, Superior stability for perovskite solar cells with 20% efficiency using vacuum co-evaporation, *Nanoscale* 9 (2017) 12316–12323.
- [17] H. Dong, J. Xi, L.J. Zuo, J.R. Li, Y.G. Yang, D.D. Wang, Y. Yu, L. Ma, C.X. Ran, W. Y. Gao, B. Jiao, J. Xu, T. Lei, F.J. Wei, F. Yuan, L. Zhang, Y.F. Shi, X. Hou, Z.X. Wu, Conjugated molecules “bridge”: functional ligand toward highly efficient and long-term stable perovskite solar cell, *Adv. Funct. Mater.* 29 (2019) 11.
- [18] L. Cojocaru, K. Wienands, T.W. Kim, S. Uchida, A.J. Bett, S. Rafizadeh, J. C. Goldschmidt, S.W. Glunz, Detailed investigation of evaporated perovskite absorbers with high crystal quality on different substrates, *ACS Appl. Mater. Interfaces* 10 (2018) 26293–26302.
- [19] J. Chen, H. Dong, L. Zhang, J. Li, F. Jia, B. Jiao, J. Xu, X. Hou, J. Liu, Z. Wu, Graphitic carbon nitride doped  $\text{SnO}_2$  enabling efficient perovskite solar cells with PCEs exceeding 22%, *J. Mater. Chem. A* 8 (2020) 2644–2653.
- [20] H. Dong, T. Lei, F. Yuan, J. Xu, Y. Niu, B. Jiao, Z. Zhang, D. Ding, X. Hou, Z. Wu, Plasmonic enhancement for high efficient and stable perovskite solar cells by employing “hot spots” Au nanobipyramids, *Org. Electron.* 60 (2018) 1–8.
- [21] D. Yang, R. Yang, J. Zhang, Z. Yang, S. Liu, C. Li, High efficiency flexible perovskite solar cells using superior low temperature  $\text{TiO}_2$ , *Energy Environ. Sci.* 8 (2015) 3208–3214.
- [22] Best Research-Cell Efficiencies (NREL). <https://www.nrel.gov/pv/assets/pdfs/best-research-cell-efficiencies.20190802.pdf>, 2019.
- [23] I.C. Smith, E.T. Hoke, D. Solis-Ibarra, M.D. McGehee, H.I. Karunadasa, A layered hybrid perovskite solar-cell absorber with enhanced moisture stability, *Angew Chem. Int. Ed. Engl.* 53 (2014) 11232–11235.
- [24] B. Conings, J. Drijkoningen, N. Gauquelin, A. Babayigit, J. D’Haen, L. D’Olieslaeger, A. Ethirajan, J. Verbeeck, J. Manca, E. Mosconi, F. De Angelis, H. G. Boyen, Intrinsic thermal instability of methylammonium lead trihalide perovskite, *Adv. Energy Mater.* 5 (2015).
- [25] M.R. Leyden, Y. Jiang, Y.B. Qi, Chemical vapor deposition grown formamidinium perovskite solar modules with high steady state power and thermal stability, *J. Mater. Chem. A* 4 (2016) 13125–13132.
- [26] X. Li, M.I. Dar, C. Yi, J. Luo, M. Tschumi, S.M. Zakeeruddin, M.K. Nazeeruddin, H. Han, M. Gratzel, Improved performance and stability of perovskite solar cells by crystal crosslinking with alkylphosphonic acid omega-ammonium chlorides, *Nat. Chem.* 7 (2015) 703–711.
- [27] M.Z. Wang, H.J. Feng, C.X. Qian, J. He, J.S. Feng, Y.H. Cao, K. Yang, Z.Y. Deng, Z. Yang, X. Yao, J.P. Zhou, S.Z. Liu, X.C. Zeng,  $\text{PbTiO}_3$  as electron-selective layer for high-efficiency perovskite solar cells: enhanced electron extraction via tunable ferroelectric polarization, *Adv. Funct. Mater.* 29 (2019) 9.
- [28] F. Bella, G. Griffini, J.P. Correa-Baena, G. Saracco, M. Gratzel, A. Hagfeldt, S. Turri, C. Gerbaldi, Improving efficiency and stability of perovskite solar cells with photocurable fluoropolymers, *Science* 354 (2016) 203–206.
- [29] J.H. Noh, S.H. Im, J.H. Heo, T.N. Mandal, S.I. Seok, Chemical management for colorful, efficient, and stable inorganic-organic hybrid nanostructured solar cells, *Nano Lett.* 13 (2013) 1764–1769.
- [30] Z.G. Tang, S. Uchida, T. Bessho, T. Kinoshita, H.B. Wang, F. Awai, R. Jono, M. M. Maitani, J. Nakazaki, T. Kubo, H. Segawa, Modulations of various alkali metal cations on organometal halide perovskites and their influence on photovoltaic performance, *Nano Energy* 45 (2018) 184–192.
- [31] D. Yang, Z. Yang, W. Qin, Y. Zhang, S. Liu, C. Li, Alternating precursor layer deposition for highly stable perovskite films towards efficient solar cells using vacuum deposition, *J. Mater. Chem. A* 3 (2015) 9401–9405.
- [32] J. Zhang, Y. Zhao, D. Yang, C. Li, S. Liu, Highly stabilized perovskite solar cell prepared using vacuum deposition, *RSC Adv.* 6 (2016) 93525–93531.
- [33] J. Ávila, C. Momblona, P.P. Boix, M. Sessolo, H.J. Bolink, Vapor-deposited perovskites: the route to high-performance solar cell production? *Joule* 1 (2017) 431–442.
- [34] S. Bonomi, D. Marongiu, N. Sestu, M. Saba, M. Patrini, G. Bongiovanni, L. Malavasi, Novel physical vapor deposition approach to hybrid perovskites: growth of  $\text{MAPbI}_3$  thin films by RF-magnetron sputtering, *Sci. Rep.* 8 (2018), 15388.
- [35] L. Qiu, S. He, Y. Jiang, D.-Y. Son, L.K. Ono, Z. Liu, T. Kim, T. Bouloumis, S. Kazaoui, Y. Qi, Hybrid chemical vapor deposition enables scalable and stable Cs-FA mixed cation perovskite solar modules with a designated area of  $91.8\text{ cm}^2$  approaching 10% efficiency, *J. Mater. Chem. A* 7 (2019) 6920–6929.
- [36] C.W. Chen, H.W. Kang, S.Y. Hsiao, P.F. Yang, K.M. Chiang, H.W. Lin, Efficient and uniform planar-type perovskite solar cells by simple sequential vacuum deposition, *Adv. Mater.* 26 (2014) 6647–6652.
- [37] M.R. Leyden, L.K. Ono, S.R. Raga, Y. Kato, S.H. Wang, Y.B. Qi, High performance perovskite solar cells by hybrid chemical vapor deposition, *J. Mater. Chem. A* 2 (2014) 18742–18745.
- [38] J. Chen, J. Xu, L. Xiao, B. Zhang, S. Dai, J. Yao, Mixed-organic-cation  $(\text{FA})_x(\text{MA})_{1-x}\text{PbI}_3$  planar perovskite solar cells with 16.48% efficiency via a low-pressure vapor-assisted solution process, *ACS Appl. Mater. Interfaces* 9 (2017) 2449–2458.
- [39] R. Sedighi, F. Tajabadi, N. Taghavinia, Vapor assisted deposition of alkaline doped perovskites: pure phase formation of  $\text{Cs}_x\text{MA}_{1-x}\text{PbI}_3$ , *Electrochim. Acta* 259 (2018) 485–491.
- [40] L. Gil-Escrig, C. Momblona, M.G. La-Placa, P.P. Boix, M. Sessolo, H.J. Bolink, Vacuum deposited triple-cation mixed-halide perovskite solar cells, *Adv. Energy Mater.* 8 (2018).
- [41] S. Du, L. Jing, X. Cheng, Y. Yuan, J. Ding, T. Zhou, X. Zhan, H. Cui, Incorporation of cesium ions into  $\text{MA}_{1-x}\text{Cs}_x\text{PbI}_3$  single crystals: crystal growth, enhancement of stability, and optoelectronic properties, *J. Phys. Chem. Lett.* 9 (2018) 5833–5839.
- [42] A. Amat, E. Mosconi, E. Ronca, C. Quarti, P. Umari, M.K. Nazeeruddin, M. Gratzel, F. De Angelis, Cation-induced band-gap tuning in organohalide perovskites: interplay of spin-orbit coupling and octahedra tilting, *Nano Lett.* 14 (2014) 3608–3616.
- [43] T. Lei, H. Dong, J. Xi, Y. Niu, J. Xu, F. Yuan, B. Jiao, W. Zhang, X. Hou, Z. Wu, Highly-efficient and low-temperature perovskite solar cells by employing a Bi-hole transport layer consisting of vanadium oxide and copper phthalocyanine, *Chem. Commun.* 54 (2018) 6177–6180.
- [44] M. Stollerfoht, C.M. Wolff, J.A. Márquez, S. Zhang, C.J. Hages, D. Rothhardt, S. Albrecht, P.L. Burn, P. Meredith, T. Unold, D. Neher, Visualization and suppression of interfacial recombination for high-efficiency large-area pin perovskite solar cells, *Nat. Energy* 3 (2018) 847–854.
- [45] R.H. Bube, Trap density determination by space-charge-limited currents, *J. Appl. Phys.* 33 (1962) 1733–1737.
- [46] S. Svanstrom, T.J. Jacobsson, T. Sloboda, E. Giangrisostomi, R. Ovsyannikov, H. Rensmo, U.B. Cappel, Effect of halide ratio and  $\text{Cs}^+$  addition on the photochemical stability of lead halide perovskites, *J. Mater. Chem. A* 6 (2018) 22134–22144.